Imaging the itinerant-to-localized transmutation of electrons across the metal-to-insulator transition in V O 3

Maximilian Thees, Min-Han Lee, Rosa Luca Bouwmeester, Pedro H
Rezende-Gonçalves, Emma David, Alexandre Zimmers, Franck Fortuna,
Emmanouil Frantzeskakis, Nicolas M Vargas, Yoav Kalcheim, et al.

Imaging the itinerant-to-localized transmutation of electrons across the metal-to-insulator transition in V₂O₃

Maximilian Thees[1], Min-Han Lee[2], Rosa Luca Bouwmeester[3], Pedro H. Rezende-Gonçalves[1,4],
Emma David[1], Alexandre Zimmers[5], Franck Fortuna[1], Emmanouil Frantzeskakis[1], Nicolas M. Vargas[2],
Yoav Kalcheim[2]†, Patrick Le Fèvre[6], Koji Horiba[7], Hiroshi Kumigashira[7,8], Silke Biermann[9,10,11],
Juan Trastoy[12], Marcelo J. Rozenberg[13], Ivan K. Schuller[2], Andrés F. Santander-Syro[1]*

In solids, strong repulsion between electrons can inhibit their movement and result in a "Mott" metal-to-insulator transition (MIT), a fundamental phenomenon whose understanding has remained a challenge for over 50 years. A key issue is how the wave-like itinerant electrons change into a localized-like state due to increased interactions. However, observing the MIT in terms of the energy- and momentum-resolved electronic structure of the system, the only direct way to probe both itinerant and localized states, has been elusive. Here we show, using angle-resolved photoemission spectroscopy (ARPES), that in V₂O₃, the temperature-induced MIT is characterized by the progressive disappearance of its itinerant conduction band, without any change in its energy-momentum dispersion, and the simultaneous shift to larger binding energies of a quasi-localized state initially located near the Fermi level.

INTRODUCTION

According to the quantum-mechanical band theory of solids, in insulators, the highest occupied band is totally filled, while in metals, it is partially filled (*1*). Thus, as temperature cannot change the number of electrons in a solid, it should not change either its intrinsic nature, i.e., metallic or insulating. Enter V₂O₃: The formal configuration of the vanadium ion would be V⁺³(3d²); hence, this oxide should be a metal. However, bulk V₂O₃ shows a first-order metal-to-insulator transition (MIT) when cooling below $T_{MIT} \approx 160$ K, with an abrupt resistivity change of more than six orders of magnitude [see Fig. 1 (A and B)] (*2–8*). Microscopically, the MIT is characterized by gap of about 750 meV opening in the optical conductivity (*9*, *10*) and is accompanied by corundum-to-monoclinic and paramagnetic to antiferromagnetic transitions (*4–7*, *11*, *12*), as illustrated in Fig. 1A. Because of the relatively localized character of the 3d orbitals, the partially filled d-bands of V₂O₃ are prone to strong electronic correlations, neglected in band theory (*2*, *7*). V₂O₃ is thus considered an archetypal system for the Mott MIT, one of the most fundamental manifestations of electron correlations, also observed in several other materials. However, after 50 years of research, the microscopic processes accompanying the Mott MIT—including the roles played by the electronic, magnetic, and structural degrees of freedom—are still controversial issues (*4–9*, *12–16*). A major reason is that an experimental imaging of the momentum-resolved changes in the electronic structure of any Mott system across the thermally induced MIT is still missing.

Previous photoemission experiments studied the momentum-integrated density of states of V₂O₃, identifying a quasiparticle (QP) peak at the Fermi level (E_F) in the metallic phase (*17*) that disappears in the insulating state (*18*) and a broad feature at a binding energy $E − E_F \approx −1.1$ eV (*19*, *20*), assigned to the lower Mott-Hubbard (MH) band (*17*, *18*). The coexistence of the QP peak and the MH band is the hallmark of the correlated state, as predicted by dynamical mean-field theory some 30 years ago (*21*). More recently, angle-resolved photoemission spectroscopy (ARPES) experiments in the metallic phase of V₂O₃ single crystals (*22*) showed the existence of an electron-like QP band around the Brillouin zone center (Γ point), dispersing down to about −400 meV over Fermi momenta $2k_F \approx 1$ Å⁻¹ along the ΓZ direction, and suggested the presence of a nondispersive component of spectral weight in the metallic QP energy region.

However, several technical challenges have hindered the realization of momentum-dependent photoemission studies of the MIT in V₂O₃. For instance, V₂O₃ crystals are extremely hard to cleave to expose a clean crystalline surface. Moreover, they become highly insulating below T_{MIT}, thus strongly charging upon electron emission, and break apart into pieces due to the structural transition. The main physical issue at stake is at the core of the strong correlations problem, namely, how electrons transmute from itinerant, wave-like objects in the metallic phase to localized particles in the insulating one. In this work, we were able to directly address this question experimentally, and we provide answers to a variety of key questions: the evolution of the Mott gap, QP dispersions, effective masses, orbital character and relative spectral weights of the QP and MH bands, and an understanding, from the viewpoint of electronic structure, of the hysteresis cycle observed in the MIT.

[1]Université Paris-Saclay, CNRS, Institut des Sciences Moléculaires d'Orsay, 91405 Orsay, France. [2]Department of Physics and Center for Advanced Nanoscience, University of California San Diego, La Jolla, CA 92093, USA. [3]Faculty of Science and Technology and MESA+ Institute for Nanotechnology, University of Twente, 7500 AE Enschede, Netherlands. [4]Departamento de Física, Universidade Federal de Minas Gerais, Av. Pres. Antonio Carlos, 6627 Belo Horizonte, Brazil. [5]LPEM, ESPCI Paris, PSL Research University, CNRS, Sorbonne Université, 75005 Paris, France. [6]Synchrotron SOLEIL, L'Orme des Merisiers, Saint-Aubin-BP48, 91192 Gif-sur-Yvette, France. [7]Photon Factory, Institute of Materials Structure Science, High Energy Accelerator Research Organization (KEK), 1-1 Oho, Tsukuba 305-0801, Japan. [8]Institute of Multidisciplinary Research for Advanced Materials (IMRAM), Tohoku University, Sendai 980-8577, Japan. [9]CPHT, CNRS, Ecole Polytechnique, Institut Polytechnique de Paris, F-91128 Palaiseau, France. [10]Collège de France, 11 place Marcelin Berthelot, 75005 Paris, France. [11]Department of Physics, Division of Mathematical Physics, Lund University, Professorsgatan 1, 22363 Lund, Sweden. [12]Unité Mixte de Physique, CNRS, Thales, Université Paris-Sud, Université Paris-Saclay, 91767 Palaiseau, France. [13]Université Paris-Saclay, CNRS, Laboratoire de Physique des Solides, 91405 Orsay, France.
*Corresponding author. Email: andres.santander-syro@universite-paris-saclay.fr
†Present address: Department of Materials Science and Engineering, Techion–Israel Institue of Technology, Haifa 3200003, Israel.
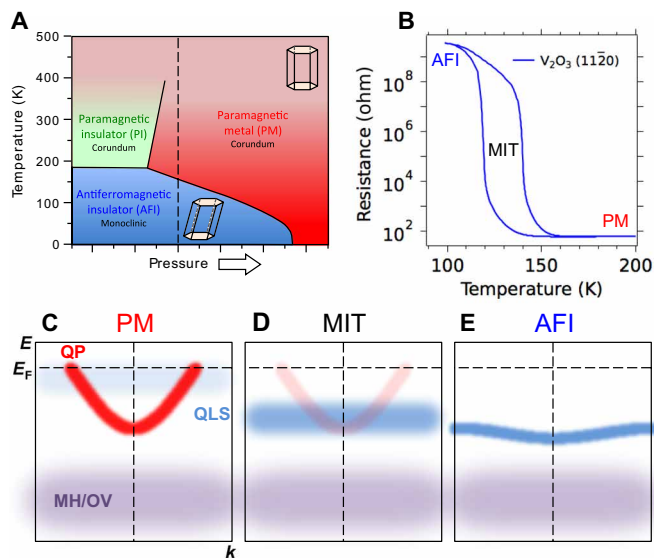
Fig. 1. V₂O₃: Schematic phase diagram and electronic structure changes. (**A**) Generic temperature-pressure phase diagram of bulk V$_2$O$_3$ (*5*). (**B**) Electrical resistance of a V$_2$O$_3$/Al$_2$O$_3$(11$\bar{2}$0) thin film studied in this work, showing the paramagnetic metal (PM), antiferromagnetic insulator (AFI), and the coexistence region across the MIT. (**C** to **E**) Schematic representation of the near-E_F electronic structure evolution observed in this work. In the PM phase, a QP band and a QLS are observed near E_F. In the coexistence region, the QP loses spectral weight without changes in dispersion, while the QLS shifts down in energy and gains spectral weight. In the AFI phase, only the QLS (showing a slight dispersion) remains, resulting in a gap below E_F.

Using ARPES, we studied high-quality crystalline thin films of V$_2$O$_3$ grown on Al$_2$O$_3$ substrates (*23–25*). Because of the anchoring imposed by the latter, the crystal integrity of the films is not affected by stress due to the structural transition. This allowed us to measure the effects of the MIT on the momentum-resolved spectral function of the system. As schematized in Fig. 1 (C to E), we found that the opening of the Mott gap at E_F in energy-momentum space happens abruptly following a gradual spectral-weight transfer: As temperature decreases in the MIT regime, there is a progressive decrease in spectral weight of an itinerant, i.e., dispersive QP conduction band, without noticeable changes in its dispersion and effective mass. This is accompanied by an energy shift, and increase in spectral weight, of a quasi-localized state (QLS), which goes from an energy close to E_F in the metallic state to an energy close to the bottom of the vanishing dispersive band in the insulating state. Only when the dispersive state crossing the Fermi level has vanished, a complete gap of about 700 meV with respect to E_F is observed, associated to the final energy position of the QLS. Furthermore, the spectral weight of the abovementioned near-E_F features shows a clear thermal hysteresis that tracks the one observed in macroscopic transport data. Another nondispersive state at lower binding energy, associated to the lower MH band, and possibly also containing a contribution from to oxygen vacancy (OV) states (see below), does not show an appreciable variation with temperature.

RESULTS AND DISCUSSION

Figure 2A shows the crystal structure of V$_2$O$_3$ both in its primitive high-temperature rhombohedral unit cell (blue) and in the associated conventional hexagonal cell (black). In rhombohedral coordinates

of the primitive cell, we write as (*hkl*) the orientation of crystallographic planes and as ⟨*hkl*⟩ the directions in reciprocal space. In hexagonal coordinates of the conventional cell, we use the four Miller indices notation, writing planes and directions, respectively, as (*hkil*) and ⟨*hkil*⟩, with $i = -h - k$.

In this work, we measured V$_2$O$_3$/Al$_2$O$_3$(11$\bar{2}$0) thin films whose surface, schematically shown in Fig. 2B, is perpendicular to the basal plane of the hexagonal cell. Complementary data on V$_2$O$_3$/Al$_2$O$_3$(01$\bar{1}$2) films are presented in the Supplementary Materials.

The surface of the V$_2$O$_3$ films was cleaned in situ using protocols previously developed for the investigation of two-dimensional (2D) electron gases in oxides (*26–30*). The cleaned surfaces showed well-defined low-energy electron diffraction (LEED) patterns (the Supplementary Materials). The cleaning process slightly lowers the onset temperature of the MIT and decreases the change in resistance between the insulating and metallic states, possibly due to the formation of OVs (*26, 27, 31, 32*), but does not affect the stoichiometry of the film nor the overall physical changes across the transition (see the Supplementary Materials). See Materials and Methods for technical details about our thin-film growth, characterization, ultrahigh-vacuum (UHV) annealing, and ARPES measurements.

Figure 2C shows the 3D rhombohedral Brillouin zone of V$_2$O$_3$ in its metallic phase, together with the 2D plane through Γ parallel to the surface of our films. For simplicity in notation, everywhere in this work, the ARPES data will be referred to directions in this particular Brillouin zone, both in the metallic and insulating phases. When relevant, the Brillouin zone edges of the monoclinic insulating structure will be indicated. The sample's surface orientation will be specified using hexagonal coordinates, as commonly done in the thin-film literature. The Supplementary Materials discusses further the rhombohedral and monoclinic Brillouin zones in relation to our ARPES data in the metallic and insulating phases.

We now present the ARPES data across the MIT. Figure 2D shows the Fermi surface map in the ($\bar{1}$10) plane of a V$_2$O$_3$/Al$_2$O$_3$(11$\bar{2}$0) thin film measured in the metallic state at T = 180 K. One observes a large Fermi sheet around the center of the Brillouin zone (Γ point). Photon energy–dependent ARPES data presented in the Supplementary Materials (in fig. S5) show that the Fermi surface disperses in the momentum direction perpendicular to the sample surface, demonstrating that the measured states are intrinsic to the bulk 3D electronic structure of the material. Figure 2E presents the corresponding energy-momentum ARPES map along $k_{\langle 111 \rangle}$, corresponding to the ΓZ direction in the rhombohedral metallic phase. The most evident features are an electron-like QP band crossing the Fermi level ($E_F = 0$) and dispersing down to about −400 meV (*18, 22*), together with a nondispersive state around an energy $E = -1.1$ eV, assigned to the lower MH band (*18*), and the valence band (VB) of oxygen p states below about $E = -4$ eV. All these features are in excellent agreement with previous photoemission and ARPES measurements in the metallic state of single crystals (*18, 22*). The clear dispersion of the QP and VBs is, moreover, an experimental proof of the crystalline quality of the thin-film surface. Note also that the MH band has most of its spectral weight concentrated at momenta around Γ, below the bottom of the QP band, similar to what has been seen previously in other correlated electron metals (*27, 33*). Part of the nondispersive spectral weight present at the same energy range as the MH band, also observed in previous ARPES works on V$_2$O$_3$ (*22*), might arise from localized states associated to the creation of OVs during the annealing process and/or ultraviolet (UV) irradiation during
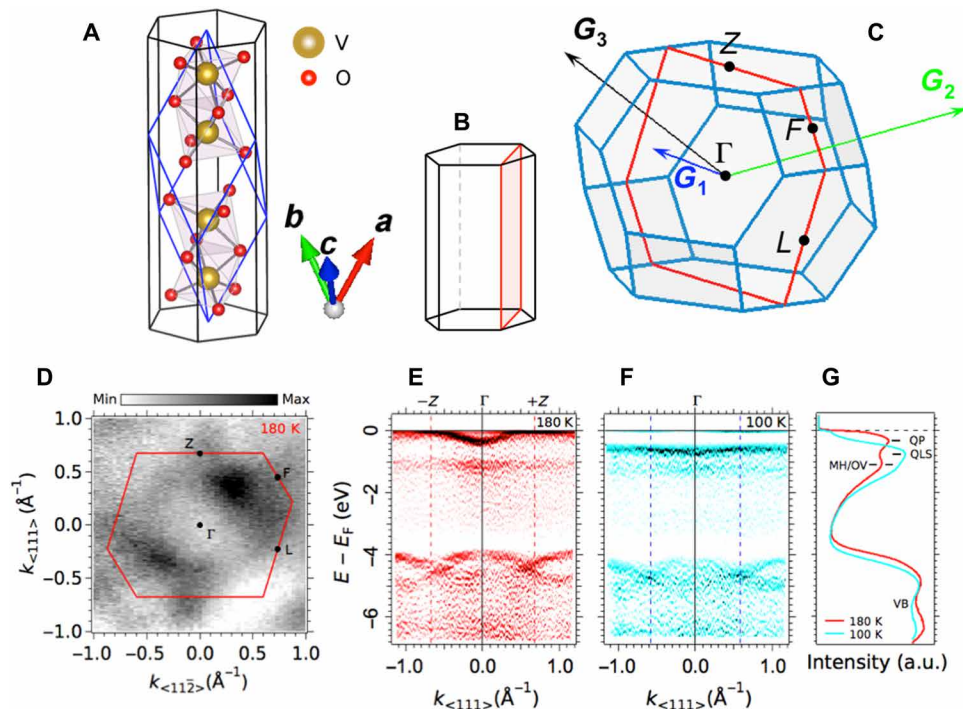
Fig. 2. V₂O₃: Crystal structure and electronic gap opening across the MIT. (**A**) Rhombohedral crystal structure of V_2O_3 (blue polyhedron) in the high-temperature metallic state. The nonprimitive hexagonal cell (black polyhedron) is also shown. (**B**) Representation of the $(11\bar{2}0)$ plane (in red) measured in this work inside the nonprimitive hexagonal cell. (**C**) Rhombohedral Brillouin zone, showing the primitive vectors of the reciprocal lattice. The $(\bar{1}10)$ plane, corresponding to a $(11\bar{2}0)$ plane in hexagonal coordinates, is shown in red. (**D**) Fermi surface map in the $\langle 111 \rangle - \langle 11\bar{2} \rangle$ plane of a thin film of $V_2O_3/Al_2O_3(11\bar{2}0)$ in the metallic state at 180 K. The rhombohedral Brillouin zone edges are marked in red. Associated high symmetry points are indicated. (**E** and **F**) Energy-momentum maps (2D curvature) along $k_{\langle 111 \rangle}$ in the metallic (180 K) and insulating (100 K) states, respectively, showing four bands: an electron-like QP band at the Fermi level, visible at 180 K; a weakly dispersive QLS at $E - E_F \approx -700$ meV, best observed at 100 K; a broad and weakly dispersing MH/OV band around $E - E_F \approx -1.1$ eV, seen at both temperatures; and the VB of oxygen p states extending from $E - E_F \approx -4$ eV downward, also present at all temperatures. The rhombohedral Brillouin zone edges ($\pm Z$ points) at 180 K and the monoclinic zone edges at 100 K are indicated by red and blue dashed lines, respectively. (**G**) Momentum-integrated raw ARPES intensities from (E) and (F), showing the QP, QLS, MH/OV, and VB states. All data were measured at a photon energy of 86 eV, corresponding to a bulk Γ point in the $\langle \bar{1}10 \rangle$ direction, using linear horizontal polarized light. The color hues in (D) to (F), as in the rest of this paper, indicate the ARPES intensity between the minimum (min) and maximum (max) detected signal. See Materials and Methods for a detailed description of the ARPES measurements and curvature analyses. a.u., arbitrary units.

experiments. Such vacancy states are commonly found at about the same binding energy, namely, $E - E_F = -1$ to -1.5 eV, in virtually all transition metal oxides (*26, 28, 29, 31, 32*), including the correlated metal $SrVO_3$, where they superpose with the MH band (*26*).

Thanks to our thin films that preserve their crystal integrity upon cooling, we can now measure the momentum-resolved spectra in the insulating phase. Figure 2F shows the energy-momentum ARPES map along $k_{\langle 111 \rangle}$ at $T = 100$ K, in the insulating state of the $V_2O_3/Al_2O_3(11\bar{2}0)$ thin film. While the VB and the MH/OV bands remain essentially unchanged, the states near E_F show a dramatic reconstruction: Instead of the strongly dispersive QP state, one observes now a weakly dispersing, previously unreported, QLS, at $E - E_F \approx -700$ meV, different from the MH/OV band. The energy of this QLS gives thus a lower bound to the Mott gap. This agrees well with the gap of about 750 to 800 meV observed in previous optical conductivity studies on V_2O_3 single crystals (*9, 10*). It also agrees with in our own infrared measurements on the same thin films used for our ARPES experiments, which show a strong decrease in reflectivity below about 800 to 900 meV in the insulating phase (fig. S3). Note that optical measurements yield the true energy gap between the highest fully occupied state, hence the QLS, and the first unoccupied state above E_F, not accessible to ARPES.

The QP, QLS, MH/OV, and VB states can also be seen in the momentum-integrated ARPES intensities (Fig. 2G). As we will see next, the QP and QLS states are a priori of different nature: The QLS is also present in the metallic phase at energies near E_F, where it coexists with the QP state—as hinted by previous ARPES work on the metallic phase of V_2O_3 single crystals (*21*). However, as the system becomes insulating, the QLS shifts down in energy and increases in intensity, while the QP state gradually loses its spectral weight.

Figure 3 shows the detailed evolution of the near-E_F electronic structure, when the temperature is first gradually lowered from the metallic (180 K) to the insulating (60 K) state, panels A to F of Fig. 3 (curvature of intensity maps) and panels L to Q of Fig. 3 (raw data), and then increased back to 180 K (Fig. 3, G to K and R to V). In the metallic state at $T \gtrsim 160$ K (Fig. 3, A, B, L, and M), the QP band can be described by a free electron–like parabola of effective mass $m^* \approx 3.5 m_e$ (m_e is the free electron mass), with its band bottom at $E_b \approx -400$ meV. The QLS, of weak intensity, can be better seen in the raw data around the Z points (near the edges of the energy-momentum maps, see also figs. S7 to S9), beyond the Fermi momenta of the QP band. Its position, at $E - E_F \gtrsim -240$ meV, is indicated by the red markers in panels L and M of Fig. 3. The MH/OV state at $E - E_F \approx -1.1$ eV is also visible—black markers in panels L and M of
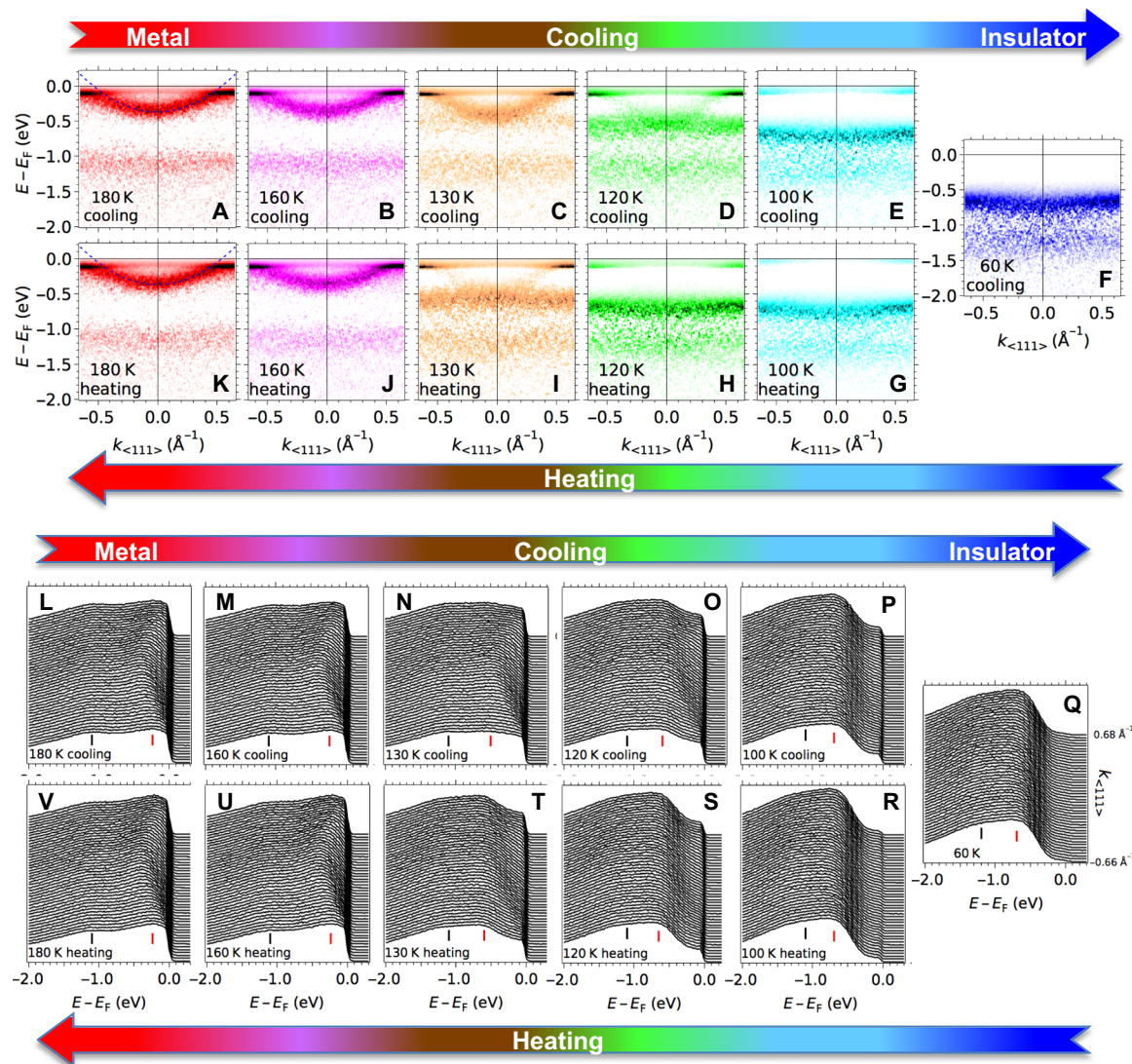
Fig. 3. Reconstruction and hysteresis of the electronic structure across the MIT. (**A** to **F**) Evolution of the ARPES energy-momentum spectra near E_F (2D curvature of intensity maps, see Materials and Methods) when cooling from 180 K (metallic state) to 60 K (insulating state) in a $V_2O_3(11\bar{2}0)$ thin film. The sharp pileup of intensity at E_F is a spurious effect of the 2D curvature analysis on the Fermi-Dirac cutoff. (**G** to **K**) Corresponding spectra when heating back to 180 K. The blue dashed parabolas in (A) and (K) represent a quasi–free electron band of effective mass $m^* \approx 3.5m_e$, assigned to the QP band. (**L** to **V**) Raw data associated to (A) to (K). Red and black markers indicate the positions of the QLS and MH/OV bands, respectively.

Fig. 3. As the sample is cooled down and enters the transition regime at 130 and 120 K (Fig. 3, C and D, and N and O), the spectral weight of the QP band decreases, without any noticeable change in its effective mass (i.e., in its energy-momentum dispersion). Simultaneously, the QLS shifts down to an energy $E \lesssim -400$ meV, becoming more intense as temperature is further lowered. In the insulating state at $T \lesssim 100$ K (Fig. 3, E and F, and P and Q), the QP band has vanished. One observes only the weakly but clearly dispersing QLS at $E - E_F \approx -700$ meV, which now shows a shallow band minimum at Γ and maxima at the monoclinic Brillouin zone edges (see also Fig. 2F) and the MH/OV band at $E - E_F \approx -1.1$ eV.

Upon heating up from the insulating state at 60 K back to the metallic state at 180 K (Fig. 3, F to K and Q to V), the spectral weight of the QLS decreases, rapidly shifting up in energy between 130 and 160 K, while the dispersive QP band reappears. A clear hysteresis in

the thermal evolution of the electronic states of the system is present, best seen in the transition regime around 120 and 130 K [compare Fig. 3 (C and D) to Fig. 3 (I and H) and Fig. 3 (N and O) to Fig. 3 (T and S)]. Thus, in the cooling cycle, the QLS becomes more apparent (with respect the QP band) below 120 K, temperature at which the QP band is still visible, while in the heating cycle, the QLS is clearly visible until 130 K, temperature at which the QP band only starts to reemerge. The energy shift of the QLS also shows differences between the cooling and heating cycles, best seen when comparing the data at 130 and 120 K. The Supplementary Materials present additional data and analyses of the thermal evolution of the near-E_F electronic structure measured in different samples.

The observation of a hysteresis in the ARPES spectra is related to the formation of phase domains in the sample, an intrinsic characteristic of first-order phase transitions. Such domains, of micrometer
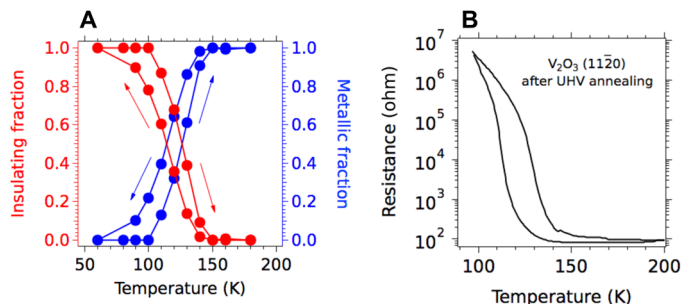
Fig. 4. Fraction of metallic and insulating electronic domains from ARPES. (**A**) Representation of the fraction of insulating and metallic domains contributing to the ARPES intensity in a V$_2$O$_3$/Al$_2$O$_3$(11$\bar{2}$0) thin film. Error bars in the fits (Eq. 1) are smaller than the size of the symbols. (**B**) Resistance as a function of temperature measured in the same sample after UHV annealing and photoemission experiments. The shift in transition temperature and the decrease of the resistivity in the insulating phase with respect to the pristine sample (Fig. 1C) are ascribed to the slight doping with OVs induced by annealing in UHV (the Supplementary Materials).

to submicrometer size, have been directly imaged in real-space in VO$_2$ and V$_2$O$_3$ by near-field infrared microscopy (*34*, *35*), photoemission microscopy (*36*), and muon spin relaxation (*37*). As the UV spot used in our experiments has a mean diameter larger than about 30 μm, the ARPES signal is a superposition of electrons emitted from both metallic and insulating phases. We then approximate the observed ARPES intensity $I(E, k, T)$ at a temperature T as a superposition of the intensity measured in the pure metallic phase ($T = 180$ K) at each energy E and wave vector k and the intensity measured in the pure insulating phase ($T = 60$ K) at the same energy and momentum. In doing so, we are assuming that, as suggested from Fig. 3, the energy shift of the QLS proceeds rather abruptly with temperature. We also neglect thermal broadening as our energy resolution (of about 15 meV) is already comparable to k_BT at 180 K. Thus, we write

$$I(E, k, T) = a(T) \times I(E, K, 180 \text{ K}) + b(T) \times I(E, k, 60 \text{ K}) \quad (1)$$

Using linear regression, we could therefore determine the phase fractions $a(T) \geq 0$ and $b(T) \geq 0$ that best fit the measured spectra for all energy and momenta, i.e., over a set of around 4×10^5 points of $I(E, k)$, at each temperature. Figure 4A shows the so-calculated fraction of insulating and metallic domains, $b/(a + b)$ and $a/(a + b)$, as a function of temperature. For comparison, the resistance obtained on the same sample after ARPES measurements (Fig. 4B) is also shown. The agreement in the hysteresis between the electrical resistance and the ARPES data (onset of the transition on cooling at around 140 to 150 K, midpoint at around 120 K, and thermal amplitude of the hysteresis of about 15 to 20 K) indicates that the observed changes in the spectral function are directly linked to the MIT.

Our temperature-dependent studies were performed along $k_{\langle 111 \rangle}$, a direction orthogonal to the antiferromagnetic wave vector in the insulating state (*11*, *12*). Hence, the band dispersions along this direction should not be directly affected by antiferromagnetic band folding. In line with this expectation, our ARPES data do not show any folding of the dispersive QP state. Instead, the spectral weight of the QP state vanishes as the system goes from metallic to insulating, without any measurable change in its dispersion, while the QLS shifts down in energy and increases in spectral weight. One possibility is

that the energy shift of the QLS, which remains essentially non-dispersing along all high-symmetry directions explored in this work (Fig. 3 and fig. S6), is associated to its nesting along momenta parallel to the antiferromagnetic wave vector. On the other hand, note that in the insulating state, the magnetic moments are ordered ferromagnetically along $k_{\langle 111 \rangle}$ (*11*). This, of course, can affect the band structure, although in a way different from antiferromagnetic folding. Future theoretical studies should address further how the specific magnetic ordering of V$_2$O$_3$ affects its different orbital states.

More generally, our ARPES measurements show that, across the MIT, the essential redistribution of spectral weight in the occupied part of the electronic spectrum occurs between the QP and QLS bands, over an energy range of about 700 meV below E_F. On the other hand, recent optical measurements show that, while a large suppression of optical conductivity occurs over an energy range of about 1 eV (*38–40*), a substantial spectral weight transfer extends up to and beyond at least 3 eV (*38*, *39*). Thus, together, ARPES and optics data indicate that the unoccupied part of the electronic spectrum is also undergoing a major reconstruction, over a large energy range of several eV, across the MIT.

Our observations of spectral weight redistribution among the QP and QLS are consistent with x-ray absorption spectroscopy measurements, which found that the metallic and insulating phases have different orbital occupancies among two states present in both phases (*41*, *42*). Our findings are also in line with multiorbital first-principles calculations for V$_2$O$_3$ (*15*, *43*, *44*). In the metallic phase, the dispersive QP band seen in the ARPES spectra and crossing the Fermi level is identified in the calculations as a band of a_{1g} dominant character, while the remaining spectral weight stems essentially from the e_g orbitals. In particular, the latter would be mainly responsible for the spectral weight of the broad QLS around E_F, as well as the Hubbard band feature around $E = -1.1$ eV. In the insulating phase, the dispersive a_{1g} band would be emptied, and only the double peak structure (at energies -0.7 and -1.1 eV) of the Hubbard band formed by the now half-filled e_g states would survive (*15*, *43*, *45*). Our data provide thus a direct, momentum-resolved illustration of the multiorbital nature of the Mott transition in V$_2$O$_3$.

MATERIALS AND METHODS
Thin film growth and characterization
The 100-nm-thick epitaxial V$_2$O$_3$ thin films were deposited on (11$\bar{2}$0)- or (01$\bar{1}$2)-oriented Al$_2$O$_3$ substrates by radio frequency magnetron sputtering, as described in a previous work (*25*). An approximately 8-mtorr ultrahigh purity Argon (>99.999%) and the growth temperature of 700°C were used during the sputtering process. The thin-film structural properties were measured using a Rigaku SmartLab x-ray diffraction system. Resistance versus temperature measurements were done using a TTPX Lakeshore cryogenic probe station equipped with a Keithley 6221 current source and a Keithley 2182A nanovoltmeter.

Crystal structure and Brillouin zone of V$_2$O$_3$
In the high-temperature metallic phase, bulk V$_2$O$_3$ crystallizes in a rhombohedral (corundum) structure, as shown in Fig. 1B, with lattice parameters $a = b = c = 5.467$ Å and angles between lattice vectors $\alpha = \beta = \gamma = 53.74°$. Such a structure can be equally represented in a nonprimitive hexagonal cell, also shown in Fig. 1 (B and C). The Miller indices (h_R, k_R, l_R) in rhombohedral coordinates are

related to the Miller indices (h_H, k_H, $i_H = -h_H - k_H$, l_H) in the corresponding hexagonal coordinates by

$$h_R = \frac{1}{3}(-k_H + i_H + l_H)$$

$$k_R = \frac{1}{3}(h_H - i_H + l_H)$$

$$l_R = \frac{1}{3}(-h_H + k_H + l_H)$$

Our thin films are grown on $Al_2O_3(11\bar{2}0)$ (*a* plane) and $Al_2O_3(01\bar{1}2)$ (*R* plane) surfaces, corresponding, respectively, to the $(\bar{1}10)$ and (011) planes in rhombohedral coordinates. Thin films grown on different Al_2O_3 surfaces present a slight distortion (at most 1% of strain) from the ideal corundum symmetry (*25*), which is negligible for ARPES measurements. Hence, in this work, we use the bulk primitive rhombohedral Brillouin zone to represent the ARPES data.

ARPES measurements

ARPES experiments were performed at the CASSIOPEE beamline of Synchrotron SOLEIL (France) and at beamline 2A of KEK-Photon Factory (KEK-PF, Japan) using hemispherical electron analyzers with vertical and horizontal slits, respectively. Typical electron energy and angular resolutions were 15 meV and 0.25°. To generate pristine surfaces for the ARPES experiments, the thin films of V_2O_3 were annealed for 5 to 10 min at approximately 550° to 600°C in UHV conditions, at a base pressure of 10^{-9} mbar before annealing, reaching a desorption peak of 8×10^{-7} mbar during annealing. LEED was used to verify the long-range crystallinity and cleanliness of our surfaces after preparation (see fig. S1). While the insulating phase of V_2O_3 would prevent the realization of ARPES experiments on a bulk sample, we found that the residual conductivity in our samples was enough to reduce the charging of the film to approximately 11 eV at 100 K under the photon flux used for our measurements. The charging was subsequently corrected by aligning the energy of the Fermi-Dirac steps (if a residual spectral weight at E_F was present) or of the VBs at all temperatures, thus assuming that such a band is not affected by the MIT. Such a hypothesis is not only physically sound, given the high binding energy of the O-2p levels that form the VB and their large separation from the MH and QP bands, but is also supported by the data that, apart from the expected thermal broadening and energy shift due to charging, do not show any notable changes in the VB shape when the system is cooled/warmed across the MIT.

Second derivative rendering of ARPES intensity maps

For second derivative rendering (fig. S5C), the raw photoemission energy-momentum maps were convolved with a 2D Gaussian of full width at half maximum of 2° in angle and 25 meV in energy to smooth the noise. Only negative values of the second derivative, representing peak maxima in the original data, are shown.

2D curvature rendering of ARPES intensity maps

The 2D curvature method (*46*) was used to enhance the intensity of broad/weak spectral features in the ARPES intensity maps. To this end, boxcar smoothing was applied to the raw data. For Fig. 2 (B and C), we used a kernel of 80 meV × 0.037 Å^{-1} with a 2D curvature free parameter of 0.2. For Fig. 3 (A to K), we used a kernel of 140 meV × 0.026 Å^{-1} with a 2D curvature free parameter of 0.1.

Only negative values of the 2D curvature, which represent maxima in the original data, are shown. After taking the 2D curvature, the data were rigidly shifted by 30 meV toward the Fermi level to preserve the exact peak positions as determined by the raw data and its second derivatives. There is no effect on the conclusions of this study as an identical shift was applied to all figures where the 2D curvature rendering is displayed.

3D *k*-space mapping

Within the free electron final state model, ARPES measurements at constant photon energy give the electronic structure at the surface of a spherical cap of radius $k = \sqrt{(2\,m_e/\hbar^2)\,(h\nu - \Phi + V_0)}$. Here, m_e is the free electron mass, Φ is the work function, and $V_0 = 12.5$ eV is the "inner potential" of V_2O_3 (*22*). Measurements around normal emission provide the electronic structure in a plane nearly parallel to the surface plane. Likewise, measurements as a function of photon energy provide the electronic structure in a plane perpendicular to the surface.

Thermal cycling in ARPES measurements

To accurately capture the electronic hysteresis behavior across the MIT, the samples were loaded into the ARPES manipulator at 200 K. Once thermalized, we performed a slow stepwise cooling cycle, setting the parameters in the temperature controller so as to avoid overshooting the set-point temperature (hence avoiding spurious hysteresis cycles) and then letting the system thoroughly thermalize at that temperature for over 30 min before measuring. After reaching the lowest measurement temperature, we performed an analogous heating cycle, measuring at the same temperatures as during the cooling cycle.

REFERENCES AND NOTES

1. N. W. Aschroft, N. Mermin, *Solid State Physics* (Brooks/Cole, 1976).
2. P. Fulde, *Correlated Electrons in Quantum Matter* (World Scientific, 2012); www.worldscientific.com/doi/pdf/10.1142/8419.
3. N. F. Mott, Metal-insulator transition. *Rev. Mod. Phys.* **40**, 677–683 (1968).
4. D. B. McWhan, T. M. Rice, J. P. Remeika, Mott transition in Cr-doped V_2O_3. *Phys. Rev. Lett.* **23**, 1384–1387 (1969).
5. D. B. McWhan, J. P. Remeika, T. M. Rice, W. F. Brinkman, J. P. Maita, A. Menth, Electronic specific heat of metallic Ti-doped V_2O_3. *Phys. Rev. Lett.* **27**, 941–943 (1971).
6. N. F. Mott, *Metal–Insulator Transitions* (Taylor and Francis, 2004).
7. M. Imada, A. Fujimori, Y. Tokura, Metal-insulator transitions. *Rev. Mod. Phys.* **70**, 1039–1263 (1998).
8. V. Dobrosavljevic, N. Trivedi, J. M. Valles Jr., *Conductor-Insulator Quantum Phase Transitions* (Oxford Univ., 2012).
9. M. J. Rozenberg, G. Kotliar, H. Kajueter, G. A. Thomas, D. H. Rapkine, J. M. Honig, P. Metcalf, Optical conductivity in mott-hubbard systems. *Phys. Rev. Lett.* **75**, 105–108 (1995).
10. M. J. Rozenberg, G. Kotliar, H. Kajueter, Transfer of spectral weight in spectroscopies of correlated electron systems. *Phys. Rev. B* **54**, 8452–8468 (1996).
11. R. M. Moon, Antiferromagnetism in V_2O_3. *Phys. Rev. Lett.* **25**, 527–529 (1970).
12. W. Bao, C. Broholm, G. Aeppli, P. Dai, J. M. Honig, P. Metcalf, Dramatic switching of magnetic exchange in a classic transition metal oxide: Evidence for orbital ordering. *Phys. Rev. Lett.* **78**, 507–510 (1997).
13. V. I. Anisimov, D. E. Kondakov, A. V. Kozhevnikov, I. A. Nekrasov, Z. V. Pchelkina, J. W. Allen, S.-K. Mo, H.-D. Kim, P. Metcalf, S. Suga, A. Sekiyama, G. Keller, I. Leonov, X. Ren, D. Vollhardt, Full orbital calculation scheme for materials with strongly correlated electrons. *Phys. Rev. B* **71**, 125119 (2005).
14. A. I. Poteryaev, J. M. Tomczak, S. Biermann, A. Georges, A. I. Lichtenstein, A. N. Rubtsov, T. Saha-Dasgupta, O. K. Andersen, Enhanced crystal-field splitting and orbital-selective coherence induced by strong correlations in V_2O_3. *Phys. Rev. B* **76**, 085127 (2007).

15. J. Trastoy, A. Camjayi, J. del Valle, Y. Kalcheim, J.-P. Crocombette, D. A. Gilbert, J. A. Borchers, J. E. Villegas, D. Ravelosona, M. J. Rozenberg, I. K. Schuller, Magnetic field frustration of the metal-insulator transition in V_2O_3. *Phys. Rev. B* **101**, 245109 (2020).

16. Y. Kalcheim, A. Camjayi, J. del Valle, P. Salev, M. Rozenberg, I. K. Schuller, Non-thermal resistive switching in Mott insulator nanowires. *Nat. Commun.* **11**, 2985 (2020).

17. S.-K. Mo, J. D. Denlinger, H.-D. Kim, J.-H. Park, J. W. Allen, A. Sekiyama, A. Yamasaki, K. Kadono, S. Suga, Y. Saitoh, T. Muro, P. Metcalf, G. Keller, K. Held, V. Eyert, V. I. Anisimov, D. Vollhardt, Prominent quasiparticle peak in the photoemission spectrum of the metallic phase of V_2O_3. *Phys. Rev. Lett.* **90**, 186403 (2003).

18. S.-K. Mo, H.-D. Kim, J. D. Denlinger, J. W. Allen, J.-H. Park, A. Sekiyama, A. Yamasaki, S. Suga, Y. Saitoh, T. Muro, P. Metcalf, Photoemission study of $(V_{1-x}M_x)_2O_3$ (M = Cr, Ti). *Phys. Rev. B* **74**, 165101 (2006).

19. S. Shin, S. Suga, M. Taniguchi, M. Fujisawa, H. Kanzaki, A. Fujimori, H. Daimon, Y. Ueda, K. Kosuge, S. Kachi, Vacuum-ultraviolet reflectance and photoemission study of the metal-insulator phase transitions in VO_2, V_6O_{13}, and V_2O_3. *Phys. Rev. B* **41**, 4993–5009 (1990).

20. K. E. Smith, V. E. Henrich, Photoemission study of composition- and temperature-induced metal-insulator transitions in Cr-doped V_2O_3. *Phys. Rev. B* **50**, 1382–1390 (1994).

21. A. Georges, G. Kotliar, Hubbard model in infinite dimensions. *Phys. Rev. B* **45**, 6479–6483 (1992).

22. I. Lo Vecchio, J. D. Denlinger, O. Krupin, B. J. Kim, P. A. Metcalf, S. Lupi, J. W. Allen, A. Lanzara, Fermi surface of metallic V_2O_3 from angle-resolved photoemission: Mid-level filling of e_g bands. *Phys. Rev. Lett.* **117**, 166401 (2016).

23. I. Valmianski, J. G. Ramirez, C. Urban, X. Batlle, I. K. Schuller, Deviation from bulk in the pressure-temperature phase diagram of V_2O_3 thin films. *Phys. Rev. B* **95**, 155132 (2017).

24. J. Trastoy, Y. Kalcheim, J. del Valle, I. Valmianski, I. K. Schuller, Enhanced metal-insulator transition in V_2O_3 by thermal quenching after growth. *J. Mater. Sci.* **53**, 9131–9137 (2018).

25. Y. Kalcheim, N. Butakov, N. M. Vargas, M.-H. Lee, J. del Valle, J. Trastoy, P. Salev, J. Schuller, I. K. Schuller, Robust coupling between structural and electronic transitions in a Mott material. *Phys. Rev. Lett.* **122**, 057601 (2019).

26. T. C. Rödel, F. Fortuna, S. Sengupta, E. Frantzeskakis, P. L. Fèvre, F. Bertran, B. Mercey, S. Matzen, G. Agnus, T. Maroutian, P. Lecoeur, A. F. Santander-Syro, Universal fabrication of 2D electron systems in functional oxides. *Adv. Mater.* **28**, 1976–1980 (2016).

27. S. Backes, T. C. Rödel, F. Fortuna, E. Frantzeskakis, P. Le Fèvre, F. Bertran, M. Kobayashi, R. Yukawa, T. Mitsuhashi, M. Kitamura, K. Horiba, H. Kumigashira, R. Saint-Martin, A. Fouchet, B. Berini, Y. Dumont, A. J. Kim, F. Lechermann, H. O. Jeschke, M. J. Rozenberg, R. Valentí, A. F. Santander-Syro, Hubbard band versus oxygen vacancy states in the correlated electron metal $SrVO_3$. *Phys. Rev. B* **94**, 241110 (2016).

28. T. C. Rödel, M. Vivek, F. Fortuna, P. Le Fèvre, F. Bertran, R. Weht, J. Goniakowski, M. Gabay, A. F. Santander-Syro, Two-dimensional electron systems in $ATiO_3$ perovskites (A=Ca, Ba, Sr): Control of orbital hybridization and energy order. *Phys. Rev. B* **96**, 041121 (2017).

29. P. Lömker, T. C. Rödel, T. Gerber, F. Fortuna, E. Frantzeskakis, P. Le Fèvre, F. Bertran, M. Müller, A. F. Santander-Syro, Two-dimensional electron system at the magnetically tunable EuO/SrTiO₃ interface. *Phys. Rev. Materials* **1**, 062001 (2017).

30. T. C. Rödel, J. Dai, F. Fortuna, E. Frantzeskakis, P. Le Fèvre, F. Bertran, M. Kobayashi, R. Yukawa, T. Mitsuhashi, M. Kitamura, K. Horiba, H. Kumigashira, A. F. Santander-Syro, High-density two-dimensional electron system induced by oxygen vacancies in ZnO. *Phys. Rev. Mater.* **2**, 051601 (2018).

31. A. F. Santander-Syro, O. Copie, T. Kondo, F. Fortuna, S. Pailhès, R. Weht, X. G. Qiu, F. Bertran, A. Nicolaou, A. Taleb-Ibrahimi, P. L. Fèvre, G. Herranz, M. Bibes, N. Reyren, Y. Apertet, P. Lecoeur, A. Barthélémy, M. J. Rozenberg, Two-dimensional electron gas with universal subbands at the surface of $SrTiO_3$. *Nature* **469**, 189–193 (2011).

32. A. F. Santander-Syro, C. Bareille, F. Fortuna, O. Copie, M. Gabay, F. Bertran, A. Taleb-Ibrahimi, P. L. Fèvre, G. Herranz, N. Reyren, M. Bibes, A. Barthélémy, P. Lecoeur, J. Guevara, M. J. Rozenberg, Orbital symmetry reconstruction and strong mass renormalization in the two-dimensional electron gas at the surface of $KTaO_3$. *Phys. Rev. B* **86**, 121107 (2012).

33. M. Takizawa, M. Minohara, H. Kumigashira, D. Toyota, M. Oshima, H. Wadati, T. Yoshida, A. Fujimori, M. Lippmaa, M. Kawasaki, H. Koinuma, G. Sordi, M. Rozenberg, Coherent and incoherent d band dispersions in $SrVO_3$. *Phys. Rev. B* **80**, 235104 (2009).

34. M. Qazilbash, M. Brehm, B.-G. Chae, P.-C. Ho, G. Andreev, B.-J. Kim, S. Yun, A. Balatsky, M. Maple, F. Keilmann, H.-T. Kim, D. Basov, Mott transition in VO_2 revealed by infrared spectroscopy and nano-imaging. *Science* **318**, 1750–1753 (2007).

35. A. McLeod, E. Heumen, J. Ramirez, S. Wang, T. Saerbeck, S. Guenon, M. Goldflam, L. Anderegg, P. Kelly, A. Mueller, M. Liu, I. Schuller, D. Basov, Nanotextured phase coexistence in the correlated insulator V_2O_3. *Nat. Phys.* **13**, 80–86 (2017).

36. S. Lupi, L. Baldassarre, B. Mansart, A. Perucchi, A. Barinov, P. Dudin, E. Papalazarou, F. Rodolakis, J. P. Rueff, J. P. Itié, S. Ravy, D. Nicoletti, P. Postorino, P. Hansmann, N. Parragh, A. Toschi, T. Saha-Dasgupta, O. K. Andersen, G. Sangiovanni, K. Held, M. Marsi, A microscopic view on the Mott transition in chromium-doped V_2O_3. *Nat. Commun.* **1**, 105 (2010).

37. B. A. Frandsen, L. Liu, S. C. Cheung, Z. Guguchia, R. Khasanov, E. Morenzoni, T. J. S. Munsie, A. M. Hallas, M. N. Wilson, Y. Cai, G. M. Luke, B. Chen, W. Li, C. Jin, C. Ding, S. Guo, F. Ning, T. U. Ito, W. Higemoto, S. J. L. Billinge, S. Sakamoto, A. Kotliar, T. Murakami, H. Kageyama, J. A. Alonso, G. Kotliar, M. Imada, Y. J. Uemura, Volume-wise destruction of the antiferromagnetic Mott insulating state through quantum tuning. *Nat. Commun.* **7**, 12519 (2016).

38. M. M. Qazilbash, A. A. Schafgans, K. S. Burch, S. J. Yun, B. G. Chae, B. J. Kim, H. T. Kim, D. N. Basov, Electrodynamics of the vanadium oxides VO_2 and V_2O_3. *Phys. Rev. B* **77**, 115121 (2008).

39. M. K. Stewart, D. Brownstead, S. Wang, K. G. West, J. G. Ramirez, M. M. Qazilbash, N. B. Perkins, I. K. Schuller, D. N. Basov, Insulator-to-metal transition and correlated metallic state of V_2O_3 investigated by optical spectroscopy. *Phys. Rev. B* **85**, 205113 (2012).

40. I. Lo Vecchio, L. Baldassarre, F. D'Apuzzo, O. Limaj, D. Nicoletti, A. Perucchi, L. Fan, P. Metcalf, M. Marsi, S. Lupi, Optical properties of V_2O_3 in its whole phase diagram. *Phys. Rev. B* **91**, 155133 (2015).

41. J.-H. Park, L. H. Tjeng, A. Tanaka, J. W. Allen, C. T. Chen, P. Metcalf, J. M. Honig, F. M. F. de Groot, G. A. Sawatzky, Spin and orbital occupation and phase transitions in V_2O_3. *Phys. Rev. B* **61**, 11506–11509 (2000).

42. F. Rodolakis, P. Hansmann, J.-P. Rueff, A. Toschi, M. W. Haverkort, G. Sangiovanni, A. Tanaka, T. Saha-Dasgupta, O. K. Andersen, K. Held, M. Sikora, I. Alliot, J.-P. Itié, F. Baudelet, P. Wzietek, P. Metcalf, M. Marsi, Inequivalent routes across the Mott transition in V_2O_3 explored by x-ray absorption. *Phys. Rev. Lett.* **104**, 047401 (2010).

43. D. Grieger, M. Fabrizio, Low-temperature magnetic ordering and structural distortions in vanadium sesquioxide V_2O_3. *Phys. Rev. B* **92**, 075121 (2015).

44. F. Lechermann, N. Bernstein, I. I. Mazin, R. Valentí, Uncovering the mechanism of the impurity-selective Mott transition in paramagnetic V_2O_3. *Phys. Rev. Lett.* **121**, 106401 (2018).

45. A. I. Poteryaev, M. Ferrero, A. Georges, O. Parcollet, Effect of crystal-field splitting and interband hybridization on the metal-insulator transitions of strongly correlated systems. *Phys. Rev. B* **78**, 045115 (2008).

46. P. Zhang, P. Richard, T. Qian, Y.-M. Xu, X. Dai, H. Ding, A precise method for visualizing dispersive features in image plots. *Rev. Sci. Instr.* **82**, 043712 (2011).

Science Advances

Imaging the itinerant-to-localized transmutation of electrons across the metal-to-insulator transition in VO

Maximilian TheesMin-Han LeeRosa Luca BouwmeesterPedro H. Rezende-GonçalvesEmma DavidAlexandre ZimmersFranck FortunaEmmanouil FrantzeskakisNicolas M. VargasYoav KalcheimPatrick Le FèvreKoji HoribaHiroshi KumigashiraSilke BiermannJuan TrastoyMarcelo J. RozenbergIvan K. SchullerAndrés F. Santander-Syro

View the article online
https://www.science.org/doi/10.1126/sciadv.abj1164
Permissions
https://www.science.org/help/reprints-and-permissions

Use of think article is subject to the Terms of service